

Electromagnetic Actuation of Microrobots in a Simulated Vascular Structure with a Position Estimator Based Motion Controller

Dingran Dong, *Student Member, IEEE*, Wah Shing Lam, and Dong Sun, *Fellow, IEEE*

Abstract— The use of microrobots to achieve micromanipulation in vivo has attracted considerable attention in recent years to meet the request of non-invasiveness, precision and high efficiency in medical treatment. This paper reports the use of a home-designed electromagnetic manipulation system to control the movements of microrobots in a simulated vascular structure. After dynamic modeling, the moving trajectory of the microrobot is designed on the basis of an artificial potential field. Estimator for position is then designed with stability analysis by a Lyapunov approach. A super-twisting algorithm is further applied to control the microrobot to move along with the desired trajectory. Simulations and experiments are finally performed to demonstrate the effectiveness of the proposed control approach.

I. INTRODUCTION

In vivo micromanipulation has received increasing attention for its broad applications such as biological process regulation, microsurgery and drug delivery, to name a few. Micromanipulation tools are designed on the basis of, for example, optical tweezers [1]–[3], chemical reactions [4]–[6], and magnetic fields [7]–[9]. Optical tweezers are highly sensitive and flexible tools that can be used to trap cells or microparticles. However, the light penetration of optical tweezers through the body is low, and thus the force of tweezers is small unless the object is transparent. Chemical reaction methods can actuate the microrobot to move forward, but chemical alteration may be induced in the body, which is difficult to control. The magnetic field method can wirelessly power and control microrobots. Under the safe magnetic field strength and appropriate exposure time, its invasiveness is much smaller than other methods. Magnetic field method is very suitable for in vivo operation. With magnetic field method, several mainstream strategies have been proposed for microrobot propulsion. Some studies designed sperm-shaped microrobots with magnetic heads and elastic tails, and used oscillating magnetic field to drive the microrobots [10]–[12]. Other studies designed the microrobot as a helical propeller that can be manipulated by a rotating magnetic field [13]–[15]. These two designs have similar properties and exhibit good

performance when the microrobots are small and the sources of magnetic field generation are far from the microrobots [16], [17]. Another commonly used manipulation method is to use magnetic field gradient to drive microrobots [18], [19]. This design has no special requirement for the shape of the microrobots for propulsion, because the driving force is directly generated by the magnetic field without the need of fluid assistant. Magnetic field gradients can be generated by permanent magnets or electromagnets. The former can be fixed together with the end-effector of the robot arm, and the control task can be achieved by changing the configuration of the robot arm [20], while the magnetic force of the latter is mainly controlled by adjusting the current through the electromagnet coils.

Several types of electromagnetic actuation systems have been developed for driving the microrobot. In [21], a five degree-of-freedom (DOF) electromagnetic system named OctoMag was designed, which was composed of eight stationary electromagnets. This system can manipulate an intraocular microrobot that can be used for delicate retinal procedures. The work [22] reported the use of scaffold-type microrobots to carry stem cells and manipulate them inside a nude mouse's intraperitoneal cavity. In these studies, motion control of the microrobots is a critical issue. Currently, many manipulation tasks are based on an open-loop control or a simple control with human-eye feedback [23]. Developing a real-time position feedback controller to precisely control microrobots under a complex environment is highly demanded. In order to detect the real-time position of ferromagnetic beads in the human body, clinical MRI systems were used in [24], [25], in which PID control and generalized predictive control were applied to ensure tracking of a predetermined trajectory. A 3-D Brownian motion control was proposed for driving a microscopic magnetic bead, with position feedback obtained by a 3-D visual tracking scheme [26], where the workspace was formed by six sharp-tipped magnetic poles connected by a magnetic yoke. In [27], a combined ISS-based control approach and nonlinear high-gain observer were developed to guarantee the stability of an electromagnetic coils system in tracking microrobots along a helix-like curve, with consideration of ubiquitous system uncertainties and disturbances.

Despite the aforementioned development in the motion control of microrobots, some challenging problems still remain unsolved, and one of which is how to obtain accurate position feedback during real-time control of microrobots. It is worth mentioning that the magnetic force applied on a microrobot is greatly dependent on the microrobot's position in the magnetic field. Even a small error in position estimation can cause large force discrepancy ($F \propto p^{-7}$). Therefore, in real time is crucial. In many applications such as drug or cell

This work was supported by a grant from the Research Grants Council of the Hong Kong Special Administrative Region, China (Ref. no. T42-409/18R), a grant from City University of Hong Kong (Ref. no. 9610443), and a grant from Shenzhen Science and Technology Project (Ref. no. R-IND 13301). (*Corresponding author*: Dong Sun.)

Dingran Dong and Wah Shing Lam are with the Department of Biomedical Engineering, City University of Hong Kong, Hong Kong, China (E-mail: drdong2-c@my.cityu.edu.hk, wahslam2-c@my.cityu.edu.hk).

Dong Sun is with the Department of Biomedical Engineering, City University of Hong Kong, Hong Kong, China and the Center for Robotics and Automation, Shenzhen Research Institute of City University of Hong Kong, Shenzhen 518057, China. (Tel.: [852] 3442-8405; Fax: [852] 3442-0176; E-mail: medsun@cityu.edu.hk).

delivery, the microrobot needs to move in a certain long distance that is beyond the field of view of microscope. Accordingly, a practical solution is proposed with a movable camera to track the position of microrobots [1]. However, without the use of a sophisticated tracking equipment, the position of camera is hard to track precisely, and thus the position of the microrobot in the magnetic field cannot be measured accurately.

To this end, we propose a motion control strategy to actuate the microrobots in a simulated vascular structure with a position estimator for compensating the error caused by inaccurate information of the camera position. Applications of microrobots to achieve targeted delivery and sensing in complex vascular network have exhibited a great potential in clinical medicine, where automatic navigation of microrobots in blood vessels represents a fundamental challenge [28]. In this paper, a path planner is designed first based on the Dijkstra algorithm. Then, a position estimator is proposed, in which the disturbances caused by the bloodstream or other unknown system dynamics are compensated. Finally, a super-twisting algorithm (STA) [29], [30] is applied as the motion control method, which is a second-order sliding mode control algorithm that can eliminate the chattering problem. Both simulations and experiments have conducted to verify that the microrobot can be automatically navigated to the desired position in a vascular structure.

II. DYNAMIC MODEL

A microparticle containing soft magnetic materials experiences a magnetic force when it is placed into the magnetic field with a magnetic field gradient $\nabla \mathbf{B} \in \mathbb{R}^2$. The magnetic force $\mathbf{F}_{mag} = [F_{mag,x}, F_{mag,y}]^T$, expressed as $\mathbf{F}_{mag} = (\mathbf{m} \cdot \nabla) \mathbf{B}$, serves as the driving force to actuate the microrobot. The magnetic moment $\mathbf{m} \in \mathbb{R}^2$ of the microrobot can be denoted as $\mathbf{m} = VT \frac{\chi}{\mu_0(1+\chi)} \mathbf{B}$, where V denotes the volume of the microrobot, χ is the susceptibility of the material, T is the ratio of magnetic material volume to the microrobot volume V . The external magnetic field has the flux density $\mathbf{B} = [B_x, B_y]^T$, which is determined by the current flow through the electromagnet with soft magnetic cores. For n electromagnets, the flux density and its gradient can be expressed as

$$\mathbf{B}(\mathbf{r}) = \sum_{i=1}^n \mathbf{B}'_i(\mathbf{r}_i) I_i, \quad (1)$$

$$\frac{\partial \mathbf{B}(\mathbf{r})}{\partial \mathbf{p}} = \sum_{i=1}^n \frac{\partial \mathbf{B}'_i(\mathbf{r})}{\partial \mathbf{p}} I_i, \quad (2)$$

where I_i is the i th current input, $\mathbf{p} = [p_x, p_y]^T$ is the position of the microrobot, and $\mathbf{B}'_i(\mathbf{r}_i)$ is the unit flux density generated by the i th electromagnet, which can be calculated by the finite element model and point dipole model [21] as

$$\mathbf{B}'(\mathbf{m}_0, \mathbf{r}) = \frac{\mu_0}{4\pi} \left(\frac{3(\mathbf{m}_0 \cdot \mathbf{r})\mathbf{r}}{|\mathbf{r}|^5} - \frac{\mathbf{m}_0}{|\mathbf{r}|^3} \right), \quad (3)$$

where $\mu_0 = 4\pi \times 10^{-7} \text{ T m/A}$ denotes the permeability of free space, $\mathbf{m}_0 \in \mathbb{R}^2$ denotes the point dipole moment, and $\mathbf{r} \in \mathbb{R}^2$ is a vector connecting the position of the microrobot and the point dipole.

When a microrobot moves in a fluidic environment at low Reynolds number, it suffers from a hydrodynamic drag force $\mathbf{F}_{drag} = [F_{drag,x}, F_{drag,y}]^T$ approximated as $\mathbf{F}_{drag} = 6\pi\eta R\mathbf{v}$, where R is the radius of the microrobot, η is the dynamic viscosity of the fluid, and $\mathbf{v} = [v_x, v_y]^T$ is the relative velocity to the fluid flow velocity \mathbf{v}_f [27]. This expression was originally used to describe the drag force of spherical objects in fluid. Our simulations conducted by using the finite element method (FEM) reveal when the microrobot is not a perfect sphere, the formula of \mathbf{F}_{drag} also holds. In most cases, the gravity should be compensated; otherwise, the microrobot will sink to the bottom of the container and then the friction force will be the dominant resistance of the movement. To solve this problem, we can use magnetic force to compensate for the gravity force in the z -direction, but this method increases the control complexity. The other solution is to set the similar density of microrobot to that of fluidic environment such that the gravity can be compensated by buoyancy. Some studies also used surfactants to reduce friction between the microrobot and channel surface in case that the gravity cannot be compensated.

According to the Newton's Second Law, the system dynamic model can be expressed as follows:

$$m \frac{d^2 \mathbf{p}}{dt^2} = \mathbf{F}_{mag} - \mathbf{F}_{drag} + \mathbf{\Delta}, \quad (4)$$

where m is the mass of the microrobot and $\mathbf{\Delta} = [\Delta_x, \Delta_y]^T$ denotes the disturbances, which may be caused by the bloodstream or other unknown system dynamics.

Consider that the microrobot has a minuscule mass. A large acceleration can be generated to make the system reach an equilibrium state quickly, such that eq. (4) can be simplified as

$$\mathbf{F}_{drag} = \mathbf{F}_{mag} + \mathbf{\Delta}. \quad (5)$$

Substituting the drag force into (5) yields a system dynamic model that can be expressed as a first-order system:

$$6\pi\eta R\mathbf{v} = \mathbf{F}_{mag} + \mathbf{\Delta}. \quad (6)$$

III. CONTROL DESIGN

To automatically guide the microrobot toward the desired position in vascular environment, the moving trajectory is designed firstly by establishing a map with an artificial potential field. Then, a controller based on estimation of the position is designed to drive the microrobot to move along such a desired trajectory precisely. Fig.1 shows the control block diagram used in this study.

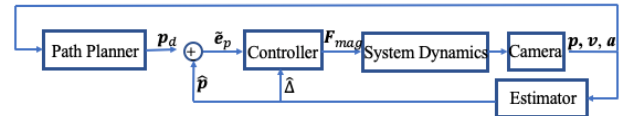


Fig.1. Control block diagram

A. Path Planner

According to [31], a global map used to distinguish the movable areas can be divided into small pieces; each piece, named a map unit window (MUW), is a set of pixel coordinates denoted by $M_{ij} = \{(x_m, y_m) | x_m, y_m \in Z, (i -$

1) $w \leq x_m < iw, (j-1)h \leq y_m < ih$. $\{x_m, y_m\}$ denotes global coordinate of the global map, where i and j are the row and column numbers, respectively. The MUW has the width of w and height of h . The microrobot can move along blood vessel toward the desired point but cannot move across the vascular wall. To find the specific areas of the intravascular and extravascular parts, the vascular wall should be detected first, which can be done by a Roberts Cross Edge Detector[32]. Depth-first-search (DFS) method can then be used to distinguish the intravascular and extravascular parts. With the DFS method, the map can be divided into moveable and unreachable areas (i.e. intravascular and extravascular parts, respectively), established as follows:

$$m_{ij} = \begin{cases} 0, & \text{moveable} \\ 1, & \text{unreachable} \end{cases}. \quad (7)$$

A distance potential field $\{D_{ij}\}$ is established by using the Dijkstra algorithm [33]. D_{ij} represents the shortest path from the current MUW to that containing the target point. The Dijkstra algorithm is used reversely. That is, the algorithm searches four directions (left, right, up, down) based on the target point, and then finds the shortest path through comparison. If $m_{ij} = 0$, then 1 is added to the distance. If $m_{ij} = 1$, then a big number exceeding the maximum distance of the whole path is added to the distance to indicate that the MUW is unreachable. Finally, the gradient of the distance potential field can be established as [31]:

$$\begin{cases} \nabla D_x(x, y) = \frac{(D_{i+1j} - D_{ij})(x - (i-1)w) + (D_{ij} - D_{i-1j})(iw - x)}{w^2} \\ \nabla D_y(x, y) = \frac{(D_{ij+1} - D_{ij})(y - (j-1)h) + (D_{ij} - D_{ij-1})(ih - y)}{h^2} \end{cases} \quad (8)$$

where $\nabla \mathbf{D}(x, y) = [\nabla D_x(x, y), \nabla D_y(x, y)]^T$ is the gradient of the distance potential field in the x and y directions, which are defined in Fig. 2, where o_{mn} is the coordinate origin when the m and n electromagnets are on. The microrobot can reach the desired position along the negative gradient direction.

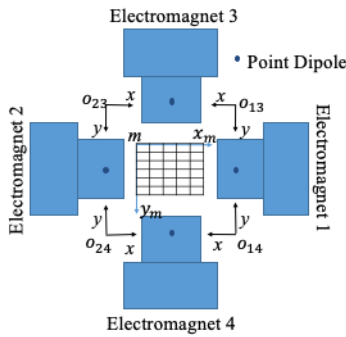


Fig. 2. Coordinate of the global map.

B. Position Estimator

Four pairwise orthogonal electromagnets are used to drive the microrobot in a horizontal x - y plane with 2 DOF. A small dish containing the microrobot is placed at the middle of the four electromagnets. To simplify the problem, point dipole moment \mathbf{m}_0 and vector \mathbf{r} are assumed to be in the same direction so that $\mathbf{m}_0 \cdot \mathbf{r} = |\mathbf{m}_0| |\mathbf{r}|$. The position of the point dipole is set to be the original point, and thus $\mathbf{r} = \mathbf{p}$. In our study, the dish is placed away from the electromagnets. When

the x -direction electromagnet is on, $p_x \gg p_y$; when the y -direction electromagnet is on, $p_y \gg p_x$. Therefore, $|\mathbf{p}| = p_\vartheta$, where $p_\vartheta, \vartheta \in \{x, y\}$. Eq. (3) can then be rewritten as

$$\mathbf{B}'(\mathbf{m}_0, p_\vartheta) = \frac{\mu_0 \mathbf{m}_0}{2\pi p_\vartheta^3}. \quad (9)$$

When the dish has a small size, the moveable range in both x - and y - directions is much smaller than the distance between the microrobot and the electromagnets. When the x -direction electromagnet is on, the field gradient along the y -direction in the microrobot moving area is small enough to be ignored. Therefore, eq.(2) can be simplified as

$$\frac{\partial \mathbf{B}(p_\vartheta)}{\partial p_\vartheta} = \sum_{i=1}^n -\frac{3\mu_0 \mathbf{m}_0}{2\pi p_\vartheta^4} I_i. \quad (10)$$

Then, the magnetic force is expressed as

$$F_{mag, \vartheta} = \sum_{i=1}^n -\frac{3}{4} VT \frac{\chi}{\mu_0(1+\chi)} \left(\frac{\mu_0 \mathbf{m}_0}{\pi}\right)^2 \left(\frac{1}{p_\vartheta^7}\right) I_i^2. \quad (11)$$

The four orthogonal electromagnets are designed to generate forces in the positive and negative directions along the x -axis and y -axis, respectively. If the microrobot moves along the x or y direction, only one power source is on. Thus, the system dynamic (6) can be expressed as

$$6\pi\eta R v_\vartheta = p_\vartheta^{-7} I^2 K_1 + \Delta_\vartheta, \quad (12)$$

where $K_1 = -\frac{3}{4} VT \frac{\chi}{\mu_0(1+\chi)} \left(\frac{\mu_0 |\mathbf{m}_0|}{\pi}\right)^2$ stays constant, $\Delta_\vartheta, \vartheta \in \{x, y\}$. In (12), the coefficient $6\pi\eta R$ can be replaced by a constant K_2 so that (12) is rewritten as $K_2 v_\vartheta = K_1 p_\vartheta^{-7} I^2 + \Delta_\vartheta$.

Then, we have

$$\dot{p}_\vartheta = v_\vartheta = \frac{K_1 p_\vartheta^{-7} I^2 + \Delta_\vartheta}{K_2}. \quad (13)$$

Taking the derivative of (13) with respect to time yields

$$\dot{v}_\vartheta = a_\vartheta = \frac{-7K_1 p_\vartheta^{-8} I^2}{K_2} v_\vartheta + \frac{2p_\vartheta^{-7} K_1 \dot{I} I}{K_2} + \frac{\dot{\Delta}_\vartheta}{K_2}. \quad (14)$$

Considering that the disturbances likely remain constant during the same experiment, we have $\dot{\Delta}_\vartheta \approx 0$.

The moving velocity \mathbf{v} can be measured directly by a CCD camera, and acceleration \mathbf{a} can be obtained on the basis of the velocity information going through a low-pass filter. Thus, a position estimator can be designed as follows:

$$\begin{aligned} \dot{\hat{p}}_\vartheta &= \hat{v}_\vartheta + L_1(a_\vartheta - \hat{a}_\vartheta) \\ &= \frac{\hat{p}_\vartheta^{-7} K_1 I^2 + \hat{\Delta}_\vartheta}{K_2} + L_1(a_\vartheta - \hat{a}_\vartheta), \end{aligned} \quad (15)$$

$$\dot{\hat{\Delta}}_\vartheta = L_2(a_\vartheta - \hat{a}_\vartheta), \quad (16)$$

where $\hat{p}_\vartheta, \hat{v}_\vartheta, \hat{a}_\vartheta$ and $\hat{\Delta}_\vartheta$ ($\vartheta \in \{x, y\}$) are estimations of the position p_ϑ , velocity v_ϑ , acceleration a_ϑ , and disturbances Δ_ϑ .

From (13)–(16) and defining $e_{p_\vartheta} = p_\vartheta - \hat{p}_\vartheta$, we have

$$\begin{aligned}
\dot{e}_{p\vartheta} &= \frac{K_1 I^2 \sum_{n=0}^6 (\hat{p}_\vartheta^n p_\vartheta^{6-n})}{K_2 \frac{p\hat{p}}{L_{k_1}(t)}} (\hat{p}_\vartheta - p_\vartheta) \\
&+ L_1 \frac{7K_1 I^2 v \sum_{n=0}^7 (\hat{p}_\vartheta^n p_\vartheta^{7-n})}{K_2 \frac{p_\vartheta \hat{p}_\vartheta}{L_{k_2}(t)}} - \frac{2K_1 I \sum_{n=0}^6 (\hat{p}_\vartheta^n p_\vartheta^{6-n})}{K_2 \frac{p_\vartheta \hat{p}_\vartheta}{L_{k_2}(t)}} \\
&(\hat{p}_\vartheta - p_\vartheta) + \frac{\Delta_\vartheta - \hat{\Delta}_\vartheta}{K_2} \\
&= -e_{p\vartheta} \underbrace{\left(\frac{L_{k_1}(t) + L_1 L_{k_2}(t)}{L_1'(t)} \right)}_{L_1'(t)} + \frac{e_{\Delta\vartheta}}{K_2}, \quad (17) \\
\dot{e}_{\Delta\vartheta} &= -\underbrace{L_2 L_{k_2}(t)}_{L_2'(t)} (\hat{p}_\vartheta - p_\vartheta) = -L_2'(t) e_{p\vartheta}, \quad (18)
\end{aligned}$$

where we have exploited $\mathbf{v} \approx \hat{\mathbf{v}}$ as \mathbf{v} is observable. As the movement range of the microrobot is known beforehand, there exist $I_{max}, p_{min}, p_{max}, \hat{p}_{min}$ and \hat{p}_{max} such that $0 < I < I_{max}$, $p_{min} < p_\vartheta < p_{max}$, and $\hat{p}_{min} < \hat{p}_\vartheta < \hat{p}_{max}$ hold. I is also set as Lipschitz continuous, and thus $I\dot{I} < K_3 I^2$. By tuning K_3 , we can achieve $L_{k_1, min} > 0, L_{k_2, min} > 0$, in $L_{k_1} \in (L_{k_1, min}, L_{k_1, max}), L_{k_2} \in (L_{k_2, min}, L_{k_2, max})$.

Given that \mathbf{v} and \mathbf{a} are observable, the convergence of e_p and e_Δ must be guaranteed. Thus, we have

$$\frac{\begin{bmatrix} \dot{e}_{p\vartheta} \\ \dot{e}_{\Delta\vartheta} \\ \dot{x} \end{bmatrix}}{\mathbf{p}} = \begin{bmatrix} -L_1' & \frac{1}{K_2} \\ -L_2' & 0 \end{bmatrix} \begin{bmatrix} e_{p\vartheta} \\ e_{\Delta\vartheta} \end{bmatrix}. \quad (19)$$

The Lyapunov function is designed as $L = \mathbf{X}^T \mathbf{H} \mathbf{X} > 0$, $\forall e_{p\vartheta}, e_{\Delta\vartheta} \neq (0,0)$, where $\mathbf{H} \in \mathbb{R}^{2 \times 2}$ is a positive definite matrix.

Taking the derivative of the Lyapunov function with respect to time leads to

$$\dot{L} = \mathbf{X}^T (\mathbf{P}^T \mathbf{H} + \mathbf{H} \mathbf{P}) \mathbf{X}. \quad (20)$$

To make \dot{L} negative definite, we choose $\mathbf{H} = \begin{bmatrix} 1 & -\frac{1}{2} \\ \frac{1}{2} & 1 \end{bmatrix}$,

and then let $\mathbf{E} = \mathbf{P}^T \mathbf{H} + \mathbf{H} \mathbf{P}$, expressed as

$$\mathbf{E} = \begin{bmatrix} -2L_1' & \frac{1}{2}L_1' - L_2' + \frac{1}{K_2} \\ -\frac{1}{2}L_1' - L_2' + \frac{1}{K_2} & 0 \end{bmatrix}. \quad (21)$$

The characteristic equation $|\lambda \mathbf{I} - \mathbf{E}|$ of \mathbf{E} is

$$\lambda^2 + 2L_1' \lambda - \left(-\frac{1}{2}L_1' - L_2' + \frac{1}{K_2} \right) \left(\frac{1}{2}L_1' - L_2' + \frac{1}{K_2} \right) = 0 \quad (22)$$

Note that L_1' and L_2' are time-varying, and their ranges can be determined by changing L_1 and L_2 . To ensure that the roots of (22) are negative, the following conditions should be satisfied:

$$2L_1' > 0 \quad (23)$$

$$-\left(\frac{1}{2}L_1' - L_2' + \frac{1}{K_2} \right) \left(-\frac{1}{2}L_1' - L_2' + \frac{1}{K_2} \right) > 0. \quad (24)$$

That is, if the condition $L_{1, min}' > 2L_{2, max}' \gg \frac{1}{K_2} > 0$ is satisfied, $\mathbf{P}^T \mathbf{H} + \mathbf{H} \mathbf{P}$ is negative definite, and thus $\dot{L} < 0$, $\forall e_{p\vartheta}, e_{\Delta\vartheta} \neq (0,0)$. Therefore, $e_{p\vartheta}$ and $e_{\Delta\vartheta}$ are asymptotically stable at the equivalence point $(0,0)$. That is, the position estimator can reliably observe the position of the microrobot and disturbances.

C. Controller

The control objective is to make the microrobot move along the designed trajectory to the desired position in the vascular structure. A second-order sliding mode control algorithm is hereby used, i.e., the super-twisting algorithm (STA) [29], [30], which can reduce the influence of noise and decrease the chattering. According to STA, we introduce the vector state variables $\mathbf{s}_1 = \tilde{\mathbf{e}}_p$ and \mathbf{s}_2 ($\mathbf{s}_1 \in \mathbb{R}^2, \mathbf{s}_2 \in \mathbb{R}^2$), which satisfy

$$\begin{aligned}
\dot{\mathbf{s}}_1 &= -b_1 |\mathbf{s}_1|^{\frac{1}{2}} \text{sign}(\mathbf{s}_1) + \mathbf{s}_2, \\
\dot{\mathbf{s}}_2 &= -b_2 \text{sign}(\mathbf{s}_1), \quad (25)
\end{aligned}$$

where b_i are the gains.

Inspired by [27], $\tilde{\mathbf{e}}_p$ is defined as the equivalent position error as follows:

$$\tilde{\mathbf{e}}_p = \begin{cases} -\nabla \mathbf{D}(x, y) \mathbf{D}'_{ij} & D_{ij} > T \\ \mathbf{p}_d - \mathbf{p} & D_{ij} \leq T \end{cases}, \quad (26)$$

where $T = \max(w, h)$ is the switching thresholds and $\mathbf{D}'_{ij} = [D'_x, D'_y]^T$ with

$$\begin{cases} D'_x = \frac{D_{i-1j}(x - (i-1.5)w) + D_{i+1j}((i+0.5)w - x)}{2w} \\ D'_y = \frac{D_{ij-1}(y - (j-1.5)h) + D_{ij+1}((j+0.5)h - y)}{2h} \end{cases} \quad (27)$$

Taking the derivative of $\mathbf{s}_1 = \tilde{\mathbf{e}}_p$ with respect to time yields

$$\begin{aligned}
\dot{\mathbf{s}}_1 &= \begin{cases} \begin{bmatrix} \left(D'_x \cdot \frac{D_{i+1j} - 2D_{ij} + D_{i-1j}}{w^2} + \nabla D_x(x, y) \cdot \frac{D_{i-1j} - D_{i+1j}}{2w} \right) v_x \\ \left(D'_y \cdot \frac{D_{ij+1} - 2D_{ij} + D_{ij-1}}{w^2} + \nabla D_y(x, y) \cdot \frac{D_{ij-1} - D_{ij+1}}{2w} \right) v_y \end{bmatrix} \\ \mathbf{v}_d - \mathbf{v} \end{cases} \\
&= \begin{cases} \mathbf{A} \mathbf{v} & D_{ij} > T \\ \mathbf{v}_d - \mathbf{v} & D_{ij} \leq T \end{cases}, \quad (28)
\end{aligned}$$

where $\mathbf{A} = -\begin{bmatrix} a & 0 \\ 0 & c \end{bmatrix}$, $\mathbf{v} = \begin{bmatrix} v_x \\ v_y \end{bmatrix}$ and \mathbf{v}_d is the desired velocity when the microrobot is close to the desired position.

From (13), (25) and (28), a controller to regulate the magnetic force can be designed as

$$\mathbf{F}_{mag} = \begin{cases} \mathbf{A}^{-1} \left(-b_1 |\mathbf{s}_1|^{\frac{1}{2}} \text{sign}(\mathbf{s}_1) + \mathbf{s}_2 \right) \cdot K_2 - \hat{\Delta} & D_{ij} > T \\ \left(\mathbf{v}_d + b_1 |\mathbf{s}_1|^{\frac{1}{2}} \text{sign}(\mathbf{s}_1) - \mathbf{s}_2 \right) \cdot K_2 - \hat{\Delta} & D_{ij} \leq T \end{cases} \quad (29)$$

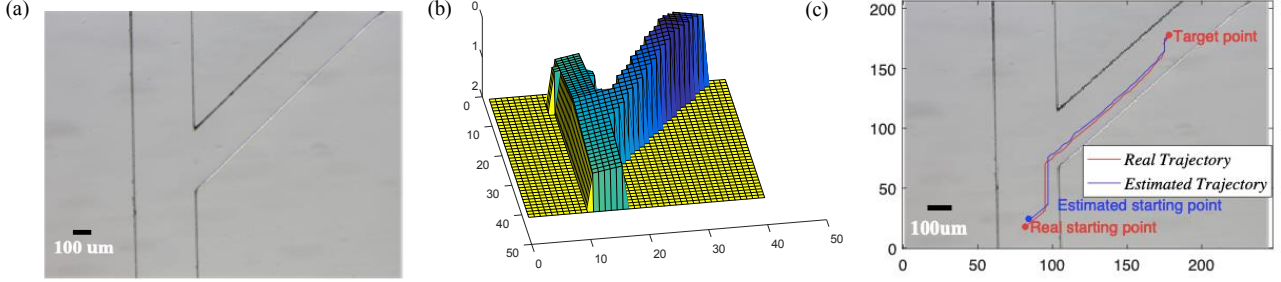


Fig. 3. Path planner. (a) Original picture. (b) Distance potential field. (c) Real and estimated trajectories in the original picture.

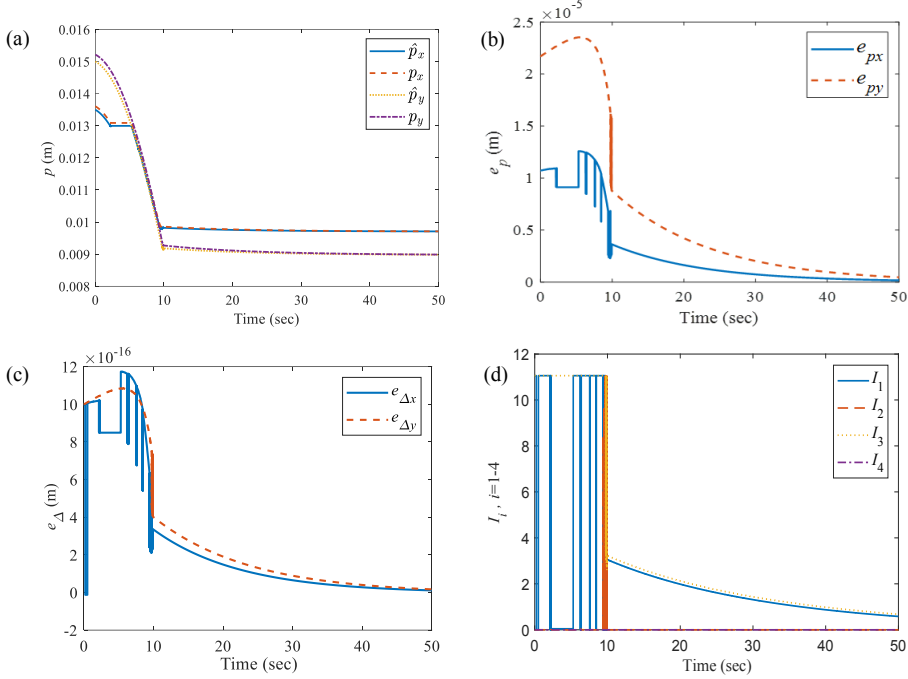


Fig. 4. Simulation results. (a) Real positions p_x (blue solid line), p_y (red dashed line) of the microrobot in the x - and y - directions and estimated positions \hat{p}_x (orange dotted line), \hat{p}_y (purple dash-dot line) of the microrobot in the x - and y - directions. (b) Position estimation errors e_{px} (blue solid line), e_{py} (red dashed line) in the x - and y - directions. (c) Disturbance estimation errors $e_{\Delta x}$ (blue solid line), $e_{\Delta y}$ (red dashed line) in the x - and y - directions. (d) Current inputs of 4 electromagnets: I_1 (blue solid line), I_2 (red dashed line), I_3 (orange dotted line), I_4 (purple dash-dot line).

With (29), the current can be calculated on the basis of the electromagnetic mode.

Under controller (29), the condition (25) is satisfied. According to the STA [29], $\mathbf{s}_1, \mathbf{s}_2$ will converge to zero in finite time with appropriate gains b_i , implying that the microrobot will move to the desired position in finite time.

IV. SIMULATIONS AND EXPERIMENTS

Simulations were performed first to verify the proposed control approach. A home-designed electromagnetic coil system has a workspace of $16 \text{ mm} \times 16 \text{ mm}$. The distance from the head of each electromagnet to the point dipole is 3.9 mm . The coordinate \mathbf{o}_{13} is selected as shown in Fig. 2. The imaging area is $10 \text{ mm} \times 8 \text{ mm}$. The moving area for the microrobot is from 6.9 mm to 16.9 mm in the x -direction and from 7.9 mm to 15.9 mm in the y -direction. The disturbance is set as $\Delta = 10^{-15} \text{ N}$, and the initial value of the estimated disturbance is zero. The diameter of the microrobot is $100 \mu\text{m}$. The thickness of Ni plating is 200 nm . In the simulations, the figure is divided into 41×41 pieces. The

control parameters are $L_1 = 0.02$, $L_2 = 8.87 \times 10^{-13}$, $b_1 = 10^{-8}$, $b_2 = 10^{-9}$, $I_{max} = 11 \text{ A}$ and $F_{max} = 1.35 \times 10^{-10} \text{ N}$. Please note that disturbances caused by unknown system dynamics may impose a steady error near the target position. Although this interference is small, it should be compensated to ensure good control performance. The following simulation and experimental results will show that the proposed robust control algorithm can overcome the disturbances caused by unknown system dynamics.

Fig. 3(a) shows the image of a vascular structure used in the simulation study, where two intravascular points ($13.6073, 15.2171$) mm and ($9.7049, 8.9732$) mm are chosen as the starting and target points, respectively. These two points are used to calculate the distance potential field as shown in Fig. 3(b). Fig. 3(c) shows the moving trajectory, where the red line denotes the desired trajectory from the starting point to the target point along the negative gradient of the distance potential field, while the blue line shows that the microrobot can move to the target point with an inaccurate starting point ($13.5000, 15.0000$) mm.

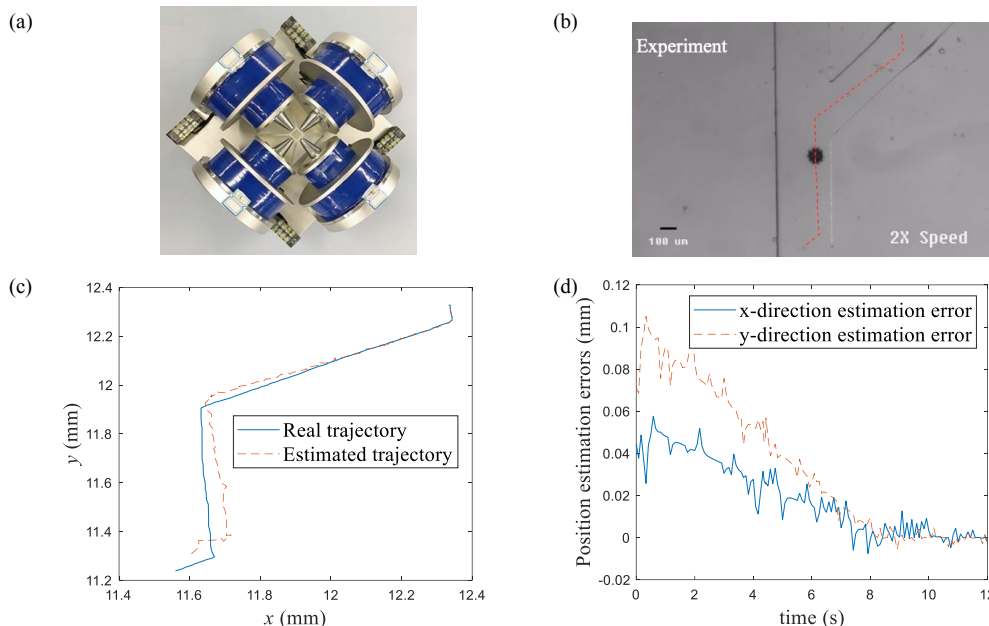


Fig. 5. Experiment setup and results. (a) The home-designed electromagnetic coil system [34]. (b) Experiment result for a microrobot's trajectory moving in a vascular structure. (c) Real and estimated trajectories for experiment. (d) Position estimation errors in the x - and y -directions.

It is seen that the actual trajectory matches the desired one very well. Fig. 4(a) shows the actual and estimated positions of the microrobot in the x - and y -directions, respectively. Fig. 4(b) shows the position estimation error. Fig. 4(c) shows the disturbance estimation error, which converges to zero. All the above results demonstrate the effectiveness of the position estimator. Fig. 4(d) shows the current input of the system, indicating that the proposed controller guarantees the current input to be within a safe limit.

In experiments, a microrobot was firstly transported into a syringe filled with phosphate buffered saline (PBS) and then injected into the microfluidic chip, which was used to mimic the vascular structure. Because the bottom of the microfluidic chip is slightly uneven, or the fluid distribution is irregular, an unbalanced force may appear between the top and bottom of the microrobot, which may trigger rotation. The magnetic force and the drag force in the horizontal direction do not change due to this rotation. By using a surfactant (Tween 20), the friction between the microrobot and the channel surface can be reduced. Therefore, the effect caused by this rotation can be ignored. A CCD camera was used to observe the movement of the microrobot. Because of the system limitation, the camera was fixed but its position was arbitrary and unknown. Therefore, the position of the microrobot in the magnetic field needs to be estimated and this experiment can also prove the effectiveness of the estimation. Fig. 5(a) shows the home-designed electromagnetic coil system used for this experiment. The ANSYS electronic desktop suite (ANSYS, USA) was used in our design and optimization process [34]. In order to evaluate and calibrate the performance of the coil, a magnetometer mounted on a micromanipulator is used to measure the magnetic field strength in the workspace, and then the measurement result is compared with the simulation result of FEM. The change of the magnetic field strength in each distance increment is expressed as a magnetic field gradient, and the magnetic field gradient is also verified by the magnetometer, which moves in 1 mm increments in the X and

Y directions. Fig. 5(b) illustrates a trajectory of the microrobot in the experiment, controlled by the proposed position estimator based motion controller. Fig. 5(c) shows the real and estimated trajectories, and their difference is shown in Fig. 5(d). It is seen that the microrobot can move along the desired trajectory successfully, thus proving the effectiveness of the proposed control strategy. It is noted that in both Fig. 5(c) and 5(d), the estimation was smoother when the microrobot approached the destination. This is because the gain of the estimator is fixed, thus when the velocity and acceleration are large, the estimation is vulnerable to estimation noise. In the future, an auto-tuned-gain estimator will be designed to improve the performance.

V. CONCLUSION

This study investigates a control strategy based on a position estimator for driving a microrobot by an electromagnetic actuation system in a simulated vascular structure. The dynamic model of the system is analyzed first, followed by the design of a moving trajectory in vascular environment. The position estimator is then developed based on the velocity information obtained by CCD camera. The estimator can reliably observe the position of the microrobot and disturbances, and the stability of the controlled system with such an estimator has been proved by a Lyapunov approach. Simulations and in vitro experiments are performed to demonstrate the effectiveness of the proposed control strategy. Due to the lack of the in vivo imaging device, the in vivo experiment was not conducted in this study. In the future work, we plan to use photoacoustic imaging technique to validate the proposed control technique in the in vivo environment and use synchronization control technique [35], [36] to achieve simultaneous control of multiple microrobots.

REFERENCES

- [1] X. Li, C. Liu, S. Chen, Y. Wang, S. H. Cheng, and D. Sun, "In vivo manipulation of single biological cells with an optical tweezers-based

- manipulator and a disturbance compensation controller," *IEEE Trans. Robot.*, vol. 33, no. 5, pp. 1200–1212, 2017.
- [2] M. Y. Xie, A. Shakoov, Y. J. Shen, J. K. Mills, D. Sun, "Out-of-plane rotation control of biological cells with a robot-tweezers manipulation system for orientation-based cell surgery," *IEEE Trans. Biomed. Eng.*, vol. 66, no. 1, pp.199–207, 2019.
 - [3] R. Diekmann, D. L. Wolfson, C. Spahn, M. Heilemann, M. Schüttelpelz, T. Huser, "Nanoscopy of bacterial cells immobilized by holographic optical tweezers," *Nat. Commun.*, vol. 7, no. 13711, 2016.
 - [4] Z. Wu, L. Li, Y. Yang, P. Hu, Y. Li, S. Yang, L. V. Wang, W. Gao, "A microrobotic system guided by photoacoustic computed tomography for targeted navigation in intestines in vivo," *Sci. Robot.*, vol. 4, no. 32, 2019.
 - [5] S. Sánchez, L. Soler, J. Katuri, "Chemically powered micro- and nanomotors," *Angew. Chem. Int. Edit.*, vol. 54, no. 5, pp. 1414–1444, 2015.
 - [6] A. A. Solovev, Y. Mei, E. Bermúdez Ureña, G. Huang, and O. G. Schmidt, "Catalytic microtubular jet engines self-propelled by accumulated gas bubbles," *Small*, vol. 5, no. 14, pp. 1688–1692, 2009.
 - [7] L. Zheng, L. Chen, H. Huang, X. Li, and L. Zhang, "An overview of magnetic micro-robot systems for biomedical applications," *Microsyst. Technol.*, vol. 22, no. 10, pp. 2371–2387, 2016.
 - [8] S. Jeon, A. K. Hoshier, K. Kim, S. Lee, E. Kim, S. Lee, et al., "A magnetically controlled soft microrobot steering a guidewire in a three-dimensional phantom vascular network," *Soft Robot.*, vol. 6, no. 1, 2019.
 - [9] P. Ryan, E. Diller, "Magnetic actuation for full dexterity microrobotic control using rotating permanent magnets," *IEEE Trans. Robot.*, vol. 33, no. 6, pp. 1398–1409, 2017.
 - [10] I. S. M. Khalil, A. F. Tabak, Y. Hamed, M. Tawakol, A. Klingner, N. E. Gohary, B. Mizaikoff, and M. Sitti, "Independent actuation of two-tailed microrobots," *IEEE Robot. Autom. Lett.*, vol. 3, no. 3, pp. 1703–1710, 2018.
 - [11] S. Sudo, S. Segawa, and T. Honda, "Magnetic swimming mechanism in a viscous liquid," *J. Intel. Mat. Syst. Str.*, vol. 17, no. 8-9, pp. 729–736, 2006.
 - [12] I. S. M. Khalil, A. F. Tabak, A. Hosney, A. Mohamed, A. Klingner, M. Ghoneima, and M. Sitti, "Sperm-shaped magnetic microrobots: fabrication using electrospinning, modeling, and characterization," in *Proc. IEEE Int. Conf. Robot. Autom.*, Stockholm, Sweden, 2016, pp. 1939–1944.
 - [13] M. A. Zeeshan, R. Grisch, E. Pellicer, K. M. Sivaraman, K.E. Peyer, J. Sort, et al., "Hybrid helical magnetic microrobots obtained by 3D template-assisted electrodeposition," *Small*, vol. 10, no. 7, pp. 1284–1288, 2014.
 - [14] A. Servant, F. Qiu, M. Mazza, K. Kostarelos, and B. J. Nelson, "Controlled in vivo swimming of a swarm of bacteria-like microrobotic flagella," *Adv. Mater.*, vol. 27, no. 19, pp. 2981–2988, 2015.
 - [15] I. S. M. Khalil, A. F. Tabak, K. Sadek, D. Mahdy, N. Hamdi, and M. Sitti, "Rubbing against blood clots using helical robots: modeling and in vitro experimental validation," *IEEE Robot. Autom. Letters*, vol. 2, no. 2, pp. 927–934, 2017.
 - [16] J. J. Abbott, K. E. Peyer, M. C. Lagomarsino, L. Zhang, L. Dong, I. K. Kaliakatsos, B. J. Nelson, "How should microrobots swim?," *Int. J. Robot. Res.*, vol. 28, no. 11-12, pp. 1434–1447, 2009.
 - [17] E. Diller, M. Sitti, "Micro-scale mobile robotics," *Found. Trends Robot.*, vol. 2, no. 3, pp. 143–259, 2013.
 - [18] K. B. Yesin, K. Vollmers and B. J. Nelson, "Modeling and control of untethered biomicrorobots in a fluidic environment using electromagnetic fields," *Int. J. Robot. Res.*, vol. 25, no. 5-6, pp. 527–536, 2006.
 - [19] J.Y. Li, X. J. Li, T. Luo, R. Wang, C. C. Liu, S. X. Chen, D. F. Li, J. B. Yue, S. Cheng, D. Sun, "Development of a magnetic microrobot for carrying and delivering targeted cells," *Sci. Robot.*, vol. 3, no. 19, 2018.
 - [20] I. S. M. Khalil, A. Alfár, A. F. Tabak, A. Klingner, S. Stramigioli, and M. Sitti, "Positioning of drug carriers using permanent magnet-based robotic system in three-dimensional space," in *Proc. IEEE/ASME Int. Conf. Adv. Intel. Mech.*, Munich, Germany, 2017, pp. 1117–1122.
 - [21] M. P. Kummer, J. J. Abbott, B. E. Kratochvil, R. Borer, A. Sengul, and B.J. Nelson, "OctoMag: An electromagnetic system for 5-DOF wireless micromanipulation," *IEEE Trans. Robot.*, vol. 26, no. 6, pp.1006–1017, 2010.
 - [22] S. Jeon, S. Kim, S. Ha, S. Lee, E. Kim, S. Y. Kim, et al., "Magnetically actuated microrobots as a platform for stem cell transplantation," *Sci. Robot.*, vol. 4, no. 30, 2019.
 - [23] N. Akçura, L. Çetin, A. Kahveci, A. K. Alasli, F. C. Can, and Ö. Tamer, "Guided motion control methodology for microrobots," in *Proc. 6th Int. Conf. Control Eng. Inf. Technol.*, Istanbul, Turkey, 2018.
 - [24] S. Tamaz, R. Gourdeau, A. Chanu, J.-B. Mathieu, and S. Martel, "Real-time MRI-based control of a ferromagnetic core for endovascular navigation," *IEEE Trans. Biomed. Eng.*, vol. 55, no. 7, pp. 1854–1863, 2008.
 - [25] K. Belharet, D. Folio, and A. Ferreira, "Endovascular navigation of a ferromagnetic microrobot using MRI-based predictive control," in *Proc. IEEE/RSSJ Int. Conf. Intel. Robot. System*, Taipei, Taiwan, 2010, pp.2804–2809.
 - [26] Z. Zhang, F. Long, and C. H. Menq, "Three-dimensional visual servo control of a magnetically propelled microscopic bead," *IEEE Trans. Robot.*, vol. 29, no. 2, pp. 373–382, 2013.
 - [27] W. C. Ma, J. Y. Li, F. Z. Niu, H. B. Ji, and D. Sun, "Robust control to manipulate a microparticle with electromagnetic coil system," *IEEE Trans. Ind. Electron.*, vol. 64, no. 11, pp. 8566–8577, 2017.
 - [28] K. Meng, Y. Jia, H. Yang, F. Niu, Y. Wang, and D. Sun, "Motion planning and robust control for the endovascular navigation of a microrobot," *IEEE Trans. Ind. Inform.*, vol. 16, no. 7, pp. 4557–4566, 2020.
 - [29] J. A. Moreno, M. Osorio, "Strict Lyapunov functions for the super-twisting algorithm," *IEEE Trans. Autom. Control*, vol. 57, no. 4, pp. 1035–1040, 2012.
 - [30] A. Levant, "Principles of 2-sliding mode design," *Automatica*, vol. 43, no. 4, pp. 576–586, 2007.
 - [31] X. J. Li, S. Xu, S. H. Cheng, and D. Sun, "Simultaneous localization and mapping-based in vivo navigation control of microparticles," *IEEE Trans. Ind. Inform.*, vol. 16, no. 5, pp. 2956–2964, 2019.
 - [32] G. T. Shrivakshan, C. Chandrasekar, "A comparison of various edge detection techniques used in image processing," *Int. J. Comput. Sci. Issues*, vol. 9, no. 1, pp. 269–276, 2012.
 - [33] D. B. Johnson, "A note on Dijkstra's shortest path algorithm," *J. ACM*, vol. 20, no. 3, pp. 385–388, 1973.
 - [34] D. F. Li, F. Z. Niu, J. Y. Li, X. J. Li, D. Sun, "Gradient-enhanced electromagnetic actuation system with a new core shape design for microrobot manipulation," *IEEE Trans. Ind. Electron.*, vol. 67, no. 6, pp. 4700–4710, 2019.
 - [35] H. Liu, J. Shan and D. Sun, "Adaptive synchronization control of multiple spacecraft formation flying", *ASME Journal of Dynamic Systems, Measurement, and Control*, vol. 129, pp. 337-342, 2007.
 - [36] D. Sun, and M. C. Tong, "A synchronization approach for the minimization of contouring errors of CNC machine tools", *IEEE Trans. Auto. Sci. Eng.*, vol. 6, no. 4, pp. 720-729, 2009.